Comparison of MISR and CERES top-of-atmosphere albedo

Wenbo Sun,[1] Norman G. Loeb,[2] Roger Davies,[3] Konstantin Loukachine,[4] and Walter F. Miller[4]

[1] The Clouds and the Earth's Radiant Energy System (CERES) and the Multi-angle Imaging SpectroRadiometer (MISR) on Terra satellite measure the Earth's top-of-atmosphere (TOA) albedo in broadband and narrowband, respectively. This study presents the first direct comparison of the CERES and MISR albedos. An algorithm for converting the MISR spectral albedos to broadband is derived. The MISR and CERES albedos for overcast ocean scenes are compared between $75°S - 75°N$ for solar zenith angles $\leq 75°$. For overcast $1° \times 1°$ ocean regions, the relative differences and the relative root-mean-square (RMS) differences between the MISR and CERES albedos are $\sim 0.8\%$ and $\sim 4.3\%$, respectively. Accounting for a $\sim 2.0\%$ error in the MISR albedos due to narrow-to-broadband albedo conversion errors, the RMS difference between the MISR and CERES albedos due to angular distribution model (ADM) differences is estimated to be $\sim 3.8\%$. The remarkable consistency between the CERES and MISR albedos for overcast oceans suggests that both instrument teams have derived accurate corrections for the radiance anisotropy of cloud scenes. This consistency will strongly enhance the confidence in the temporal trends of cloud albedo measured by the CERES and have significant impact on climate studies. **Citation:** Sun, W., N. G. Loeb, R. Davies, K. Loukachine, and W. F. Miller (2006), Comparison of MISR and CERES top-of-atmosphere albedo, *Geophys. Res. Lett.*, *33*, L23810, doi:10.1029/2006GL027958.

1. Introduction

[2] The broadband albedo of the Earth, defined as the percentage fraction of incident solar radiation reflected by the Earth, is a fundamental climate parameter. A gradual change in global albedo of only 0.002 per decade is equivalent in magnitude to the current 0.6 Wm^{-2} per decade anthropogenic total radiative forcing [*Intergovernmental Panel on Climate Change*, 2001]. One of the challenges involved in determining albedo from satellite instruments is the conversion of measured radiances to radiative fluxes, from which albedo is derived. *Suttles et al.* [1992] has shown that the radiance-to-flux conversion problem was a major source of error in the Earth Radiation Budget Experiment (ERBE) [*Barkstrom*, 1984]. One of the goals of the

Clouds and the Earth's Radiant Energy System (CERES) experiment [*Wielicki et al.*, 1996, 1998] was to significantly improve the accuracy of satellite-derived TOA fluxes by developing new empirical Angular Distribution Models (ADMs) from the CERES broadband radiance measurements and the Moderate Resolution Imaging Spectroradiometer (MODIS) [*King et al.*, 1992] cloud property retrievals [*Loeb et al.*, 2005]. Recent validation studies [*Loeb et al.*, 2006a, 2006b] confirm that radiative flux accuracy has improved with the new CERES ADMs by at least a factor of 2 over the ERBE, and that systematic angle-dependent biases in the ERBE global albedo are not present when the new CERES ADMs are used.

[3] An alternate approach for estimating albedo is to use a "simultaneous" multi-angle observing strategy, in which measurements from a region at more than one angle are acquired within a period of several minutes [*Buriez et al.*, 1997; *Diner et al.*, 1999]. The Multi-angle Imaging SpectroRadiometer (MISR) [*Diner et al.*, 1998] on Terra views the Earth by measuring the intensity of reflected sunlight at nadir and 26°, 46°, 60°, and 70° forward and backward of nadir along the spacecraft track, at four spectral bands: 0.446 μm (Blue), 0.558 μm (Green), 0.672 μm (Red), and 0.866 μm (NIR). A unique feature of the MISR is that albedos are derived from nine near-simultaneous measurements of the same target instead of just one angle [*Diner et al.*, 1999]. Furthermore, the MISR albedos are derived at a higher spatial resolution than has been hitherto possible.

[4] By necessity, deriving albedos from either the CERES or MISR radiance measurements involves making a correction for the angular dependence of the radiance field. The objective of this paper is to examine the consistency between TOA albedos from the CERES and MISR. Since the CERES and MISR teams have developed independent approaches for estimating TOA albedo, this is a unique opportunity to assess how the two albedo datasets compare with each other. To perform the comparison, it is first necessary to derive a narrowband-to-broadband albedo conversion algorithm to convert the MISR spectral albedos to broadband. Section 3 describes the algorithm used here based on a new CERES-MISR-MODIS dataset. Using the narrowband-to-broadband albedo conversion algorithm, the MISR spectral albedos from the MISR Level-2 TOA/Cloud Albedo Data product are converted into broadband albedos and compared with the CERES broadband albedos. In this initial study, we restrict the analysis to overcast ocean scenes.

2. Observations

[5] The CERES, MODIS, and MISR instruments aboard NASA's Terra satellite make critical measurements of cloud and aerosol properties and their effects on the solar radiation budget and global climate. A combination of the CERES

[1] Center for Atmospheric Sciences, Hampton University, Hampton, Virginia, USA.
[2] NASA Langley Research Center, Hampton, Virginia, USA.
[3] Department of Physics, University of Auckland, Auckland, New Zealand.
[4] Science Applications International Corporation, Hampton, Virginia, USA.

and MODIS measurements is used to produce the Single Scanner Footprint TOA/Surface Fluxes and Clouds (SSF) data product (E. B. Geier et al., Single satellite footprint TOA/surface fluxes and clouds (SSF) collection document, 2001, available at http://asd-www.larc.nasa.gov/ceres/collect_guide/SSF_CG.pdf). Recently, the multi-angle and multi-channel radiances of the MISR Level-1B2 ellipsoid-projected data were merged with the CERES SSF dataset by convolving measurements in each of the nine MISR angles with the CERES point spread function (PSF) [*Loeb et al.*, 2006b]. The merged SSF and MISR dataset (SSFM) provides coincident measurements of spectral radiance from the MISR and MODIS together with broadband radiances from the CERES. This makes it possible to convert the MISR spectral radiances at the 9 viewing angles into shortwave (SW) radiances, which is the initial step for converting narrowband MISR albedos to broadband albedos.

[6] MISR produces three spectral albedo products [*Diner et al.*, 1999]. Local albedos are estimates of the reflected flux passing through an unobscured dynamically variable reflecting level reference altitude (RLRA) at 2.2-km resolution. The restrictive albedo is closer to the ERBE or CERES definition of albedo, and is an estimate of the reflected flux that originates from the reflecting surfaces within the region. The expansive albedo is an estimate of the flux passing through the TOA irrespective of where it originates. Both expansive and restrictive albedos make use of ADMs obtained at the local albedo level. In this study, the 35.2-km restrictive albedos from the MISR Level-2 TOA/Cloud Albedo Data product are used.

3. Conversion of MISR Spectral Albedos to Broadband Albedos

[7] The MISR Level-2 spectral albedos are converted to broadband albedos by applying a conversion scheme which firstly requires the conversion of the MISR spectral reflectances from the SSFM dataset to broadband reflectances. Thereafter, the spectral and broadband reflectances at the 9 MISR viewing angles are extended to other angles and are integrated over angle to obtain generic spectral and broadband albedos. A linear spectral-to-broadband regression of the generic albedos generates the coefficients for the conversion of the MISR Level-2 spectral albedos to broadband albedos.

[8] *Loeb et al.* [2006b] used the SSFM dataset to perform a linear regression analysis for converting spectral reflectances at each of the 9 MISR viewing angles into broadband reflectances. In this study, for each viewing direction the MISR spectral reflectances in the red and near-infrared (NIR) bands are related to the CERES SW reflectance as follows:

$$R_{sw} = c_0 + c_1 R_{red} + c_2 R_{nir}, \qquad (1)$$

where R_{sw}, R_{red}, and R_{nir} are the CERES SW reflectance, the MISR red reflectance, and the MISR NIR reflectance, respectively, and c_0, c_1, and c_2 are coefficients of the regression analysis defined as a function solar zenith angle, viewing zenith angle, relative viewing azimuth angle, cloud fraction, effective cloud top pressure, precipitable water, and surface scene-type. The solar zenith angle and viewing zenith angle are stratified into 10° bins and relative viewing

azimuth angle into 20° bins. Cloud fraction is stratified into 11 bins from 0% to 100% with an increment of 10%. The uncertainty in broadband reflectance based on the narrow-to-broadband algorithm are generally small, with a relative bias error of ∼0.25%, and a relative root-mean-square (RMS) error of ∼3% for overcast or clear footprints. For broken cloud conditions, the error is larger, reaching ∼6%. Note that using the blue- and green-band data of the MISR may slightly reduce the uncertainty in the narrow-to-broadband reflectance conversion over clear scenes. However, our tests show that for cloudy scenes the errors of the narrow-to-broadband reflectance regression are only insignificantly decreased by using additional data such as the blue and green radiances.

[9] To estimate reflectances at angles that are not sampled by the MISR, we use the following approximation:

$$\hat{R}(\theta_0, \theta, \phi) = [R_t(\theta_0, \theta, \phi, \tau, f)/R_t(\theta_0, \theta_i, \phi_i, \tau, f)] \cdot R(\theta_0, \theta_i, \phi_i), \qquad (2)$$

where $\hat{R}(\theta_0, \theta, \phi)$ denotes the estimate of spectral or SW reflectance at solar zenith angle θ_0, viewing zenith angle θ, and relative azimuth angle ϕ, $R(\theta_0, \theta_i, \phi_i)$ denotes the spectral or SW reflectance at the MISR viewing angle (θ_i, ϕ_i), and R_t corresponds to a theoretical reflectance evaluated at cloud fraction f and cloud optical depth τ. Here, (θ_i, ϕ_i) is chosen to be the MISR viewing angle closest to (θ, ϕ) amongst the 9 viewing directions. The theoretical spectral or broadband radiance for a given f and τ is determined from:

$$R_t(\theta_0, \theta, \varphi, \tau, f) = (1-f)R_d(\theta_0, \theta, \varphi, 0) + fR_d(\theta_0, \theta, \varphi, \tau), \quad (3)$$

where $R_d(\theta_0, \theta_n, \varphi, \tau)$ denotes the reflectance calculated by the discrete ordinate radiative transfer model (DISORT) [*Stamnes et al.*, 1988] for a plane parallel cloud. In equation (2), the theoretical model provides a factor (ratio of reflectances) to scale observations in bins where data are available $((\theta_i, \phi_i))$ and estimate spectral and broadband reflectances in unsampled bins $((\theta, \phi))$. Cloud fraction in equation (3) is obtained from the SSF (based on the MODIS radiances within a CERES footprint), while τ is a free-variable, selected by minimizing the following [*Sun et al.*, 2004]:

$$s^2(\theta_0, \tau, f) = \sum_{n=1}^{9} [R_m(\theta_0, \theta_n, \varphi_n) - R_t(\theta_0, \theta_n, \varphi_n, \tau, f)]^2, \quad (4)$$

where $R_m(\theta_0, \theta_n, \varphi_n)$ denotes the reflectance measured by the MISR camera n. The cloud model which produces the smallest red and NIR $s^2(\theta_0, \tau, f)$ sum is used in equation (2) along with the MISR observations to estimate red, NIR and SW reflectances at all other viewing angles.

[10] The plane-parallel model calculations consist of red, NIR and SW reflectances stored in look-up tables for the following cloud optical depths: 0.0, 1.25, 8.75, 12.5, 17.5, 22.5, 27.5, 32.5, and 37.5. The calculations are based on the DISORT with a correlated-k algorithm for broadband calculation [*Kato et al.*, 1999]. We assume a water cloud layer at 1–2 km over the ocean surface. The ocean surface is represented using the *Cox and Munk* [1956] model with a surface wind speed of 7 ms^{-1}. The ocean bidirectional reflectance distribution function (BRDF) model used for
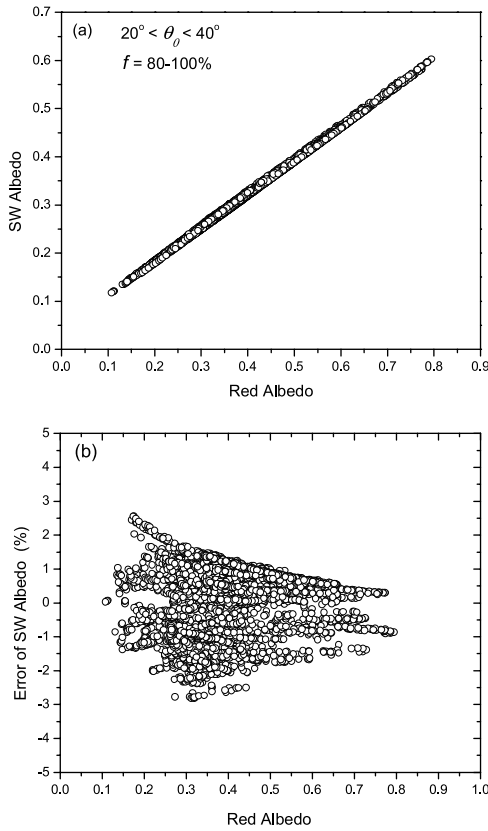
Figure 1. (a) The broadband albedo and (b) the error in the albedo narrow-to-broadband regression as function of the MISR red-channel albedo for a solar zenith angle range of 20° to 40° and a cloud fraction range of 80–100%, respectively, derived from the SSFM data of November 7, 2000.

the computation is provided by *Vermote et al.* [1997]. The water droplets in the layer of water cloud are assumed to have a lognormal size distribution with an effective radius of 10 μm. The aerosol optical thickness is assumed to be 0.075.

[11] The reflectances are integrated over angle to determine generic narrowband and broadband albedos. A narrow-to-broadband albedo regression is then produced from:

$$\alpha_{sw} = b_0 + b_1\alpha_{red} + b_2\alpha_{nir}, \qquad (5)$$

where α_{sw}, α_{red}, and α_{nir} are the SW, red, and NIR albedos, respectively. The regression coefficients b_0, b_1, and b_2 are determined using all the CERES footprints from 25 days of the SSFM data. Figure 1 provides an example of broadband albedo as function of the red-channel albedo for $f = 80–100\%$ using the SSFM data of November 07, 2000, with solar zenith angle θ_0 between 20° and 40°. As shown, the narrowband and broadband albedos have linear relation-

ship. The coefficients b_0, b_1, and b_2 are defined solely as functions of solar zenith angle because their dependence on cloud conditions is weak. Table 1 provides the actual values of b_0, b_1, and b_2 used in this study for the different solar zenith angle bins. Also shown are the relative RMS uncertainty of the conversion and the sample number for each solar zenith angle bin. The relative RMS errors for solar zenith angles between 30° and 80° are generally between 1% and 3% and tend to increase close to the terminator. For solar zenith angles <30°, the sampling size is limited due to the Terra orbit. Therefore, for this solar zenith angle range narrow-to-broadband coefficients for $30° \le \theta_0 \le 40°$ are used.

4. Results

[12] Using the narrow-to-broadband relationship for albedo from equation (5), the MISR red and NIR albedos in the MISR Level-2 TOA/Cloud Albedo Data are converted to broadband albedos and compared with broadband albedos derived from the CERES SSF data. Note that the MISR restrictive albedo is derived at dynamically variable RLRA [*Diner et al.*, 1999] and the CERES albedo is defined at a given reference level of 20 km [*Loeb et al.*, 2002]. Because of the finite geometry of the Earth, the outgoing flux varies as the inverse square of the distance from the center of the Earth, due to the fact that a change in flux reference level simply changes the surface area over which the outgoing radiant energy is distributed. Therefore, different flux reference level results in slightly different outgoing flux. In order to account for this difference, the reference level of the CERES albedos is adjusted from 20 km to the MODIS-based cloud-top height (h) using the inverse-square law:

$$\alpha = \left(\frac{r_e + 20}{r_e + h}\right)^2 \alpha_{SSF}, \qquad (6)$$

where α_{SSF} denotes the CERES SW albedo directly from the CERES SSF data (with a 20-km reference level), and r_e is Earth's radius (= 6378.137 km). The MISR and CERES albedos are sorted into $1° \times 1°$ latitude-longitude regions over ocean and averaged as follows:

$$\overline{\alpha} = \frac{\sum_{i=1}^{n} \alpha_i \cos\theta_{0i}}{\sum_{i=1}^{n} \cos\theta_{0i}}, \qquad (7)$$

where n denotes the number of MISR Level 2 35.2-km region or CERES footprints inside the $1° \times 1°$ region; α_i and θ_{0i} denote the SW albedo and solar zenith angle, respectively, at the *i-th* MISR Level 2 35.2-km region or

Table 1. Coefficients b_0, b_1, and b_2 for Conversion of MISR Red and NIR Spectral Albedo to Broadband Albedo Using , With Sample Number and RMS Uncertainty of the Conversion for Each Solar Zenith Angle Bin

| θ_0	b_0	b_1	b_2	Number of Samples	RMS, %
00°–40°	0.41833E-01	0.54756E+00	0.15144E+00	176635	1.3
40°–50°	0.39479E-01	0.32979E+00	0.37592E+00	429073	2.1
50°–60°	0.35775E-01	0.72601E+00	0.10084E-04	419692	2.3
60°–70°	0.31889E-01	0.63807E+00	0.10235E+00	311992	2.4
70°–80°	0.21622E-01	0.84271E+00	−0.71137E-01	149448	2.9
80°–90°	0.16645E-01	0.76100E+00	0.77291E-01	30545	6.4
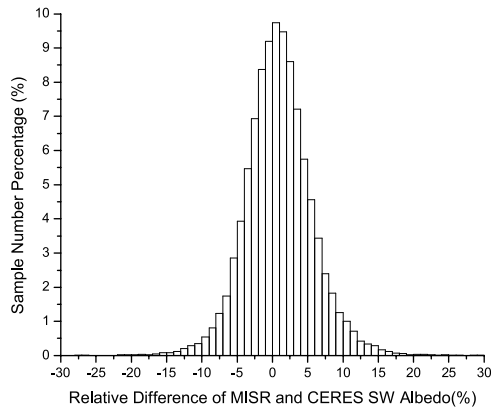
Figure 2. The percentage of $1° \times 1°$ region (sample) number as a function of the relative difference between the MISR and CERES albedo (i.e. $100\% \times [\bar{\alpha}_{MISR} - \bar{\alpha}_{CERES}]/\bar{\alpha}_{CERES}$) for overcast ocean scenes in October 2001, for solar zenith angles $\leq 75°$.

CERES footprint in the $1° \times 1°$ region. To ensure a simultaneous comparison of the MISR and CERES albedos, only the $1° \times 1°$ regions over which the difference between the mean cosine of the MISR and CERES solar zenith angles is smaller than 0.005 are considered. Also, to reduce spatial sampling differences between the CERES and MISR within the $1° \times 1°$ regions, we use albedos derived from the CERES instrument in cross-track mode and only consider footprints that lie within the MISR swath. Furthermore, only

$1° \times 1°$ regions with more than 2 MISR Level-2 35.2-km regions and more than 12 CERES footprints are considered.

[13] Figure 2 shows a histogram of the relative difference between the MISR and CERES SW albedos (i.e., $100\% \times [\bar{\alpha}_{MISR} - \bar{\alpha}_{CERES}]/\bar{\alpha}_{CERES}$) for $1° \times 1°$ overcast ocean regions in October 2001, for solar zenith angles $\leq 75°$. The cloud conditions of these regions are based on the MODIS data. The peak of the distribution occurs at $\sim 1\%$, with $\sim 82\%$ of the population between $\pm 5\%$. Overall, the relative difference between the instantaneous $1° \times 1°$-region-averaged MISR and CERES albedos is $\sim 0.8\%$. The RMS difference between the instantaneous $1° \times 1°$-region-averaged MISR and CERES albedos is 4.3%. The instantaneous RMS differences are due to a combination of the ADM differences, spatial sampling differences between the MISR Level-2 35.2-km regions and the CERES footprints within $1° \times 1°$ regions, and narrow-to-broadband conversion errors. Our tests show that, for $1° \times 1°$ regions with more than 2 MISR Level-2 35.2-km regions and more than 12 CERES footprints, different number of MISR Level-2 35.2-km regions and CERES footprints can cause a $<\sim 0.5\%$ change in overall RMS difference. Therefore, spatial sampling errors are estimated to be $<\sim 0.5\%$, while narrow-to-broadband albedo conversion errors are estimated to be $\sim 2.0\%$ (Table 1). Therefore, the RMS difference between the MISR and CERES albedos due to the ADM differences alone is $\sim 3.8\%$. By comparison, the best estimate of the CERES TOA albedo error due to the ADM uncertainties is 3% [*Loeb et al.*, 2006a].
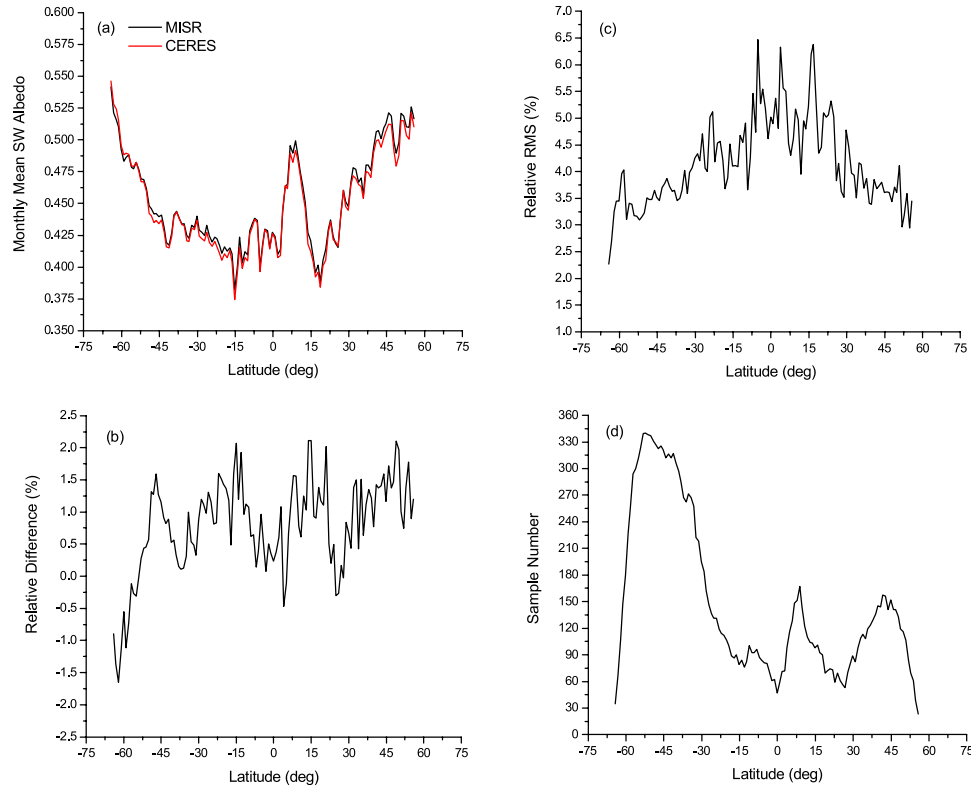
Figure 3. (a) The monthly zonal mean of the MISR and CERES albedos for overcast ocean scenes in October 2001, for solar zenith angles $\leq 75°$; (b) the monthly zonal mean of the relative differences between the instantaneous $1° \times 1°$-region-averaged MISR and CERES albedos; (c) the monthly zonal mean of the relative RMS differences between the instantaneous $1° \times 1°$-region-averaged MISR and CERES albedos; and (d) zonal $1° \times 1°$ region sample numbers.

[14] Figure 3a shows the monthly zonal mean MISR and CERES SW albedos for overcast ocean regions in October 2001, for solar zenith angles ≤75°; and Figure 3b shows the corresponding relative difference between the two. Relative differences generally lie between ±2% and show no systematic dependence upon latitude. Figure 3c shows the zonal relative RMS difference between the MISR and CERES instantaneous albedos derived from $1° \times 1°$ daily means. The relative RMS differences increase from ~3% in the midlatitudes to ~6% close to the equator, where the sampling is lower as shown in Figure 3d.

5. Conclusions

[15] The objective of this paper is to examine the consistency between TOA albedos from the CERES and MISR. To determine TOA broadband albedos from the MISR spectral albedos in the MISR Level-2 TOA/Cloud Albedo Data product, a narrow-to-broadband albedo conversion algorithm is developed. The MISR SW albedos derived from the narrow-to-broadband albedo conversion algorithm are compared with the CERES TOA SW albedos for overcast $1° \times 1°$ latitude-longitude ocean regions. The overall relative difference between the MISR and CERES albedos for 75°S−75°N and solar zenith angles ≤75° is ~0.8%, and the instantaneous relative RMS difference derived from coincident MISR and CERES albedos in $1° \times 1°$ latitude-longitude regions is ~4.3%. Given that ~0.5% difference is due to CERES-MISR spatial sampling errors, and ~2.0% is due to the MISR narrow-to-broadband albedo conversion errors, the RMS difference between the MISR and CERES albedos due to the ADM differences alone is ~3.8%. The remarkable consistency between the CERES and MISR albedos for overcast scenes suggests that both instrument teams have derived accurate corrections for the radiance anisotropy of cloud scenes. This consistency is a substantial demonstration of the accuracy of the CERES ADMs. It will strongly enhance the confidence in the temporal trends of cloud albedo measured by the CERES and have significant impact on climate studies.

References

Barkstrom, B. R. (1984), The Earth Radiation Budget Experiment (ERBE), *Bull. Am. Meteorol. Soc.*, *65*, 1170–1186.

Buriez, J. C., C. Vanbauce, F. Parol, P. Goloub, M. Herman, B. Bonnel, Y. Fouquart, P. Couvert, and G. Seze (1997), Cloud detection and derivation of cloud properties from POLDER, *Int. J. Remote Sens.*, *18*, 2785–2813.

Cox, C., and W. Munk (1956), Slopes of the sea surface deduced from photographs of the sun glitter, *Bull. Scripps Inst. Oceanogr.*, *6*, 401–488.

Diner, D. J., et al. (1998), Multiangle Imaging SprectroRadiometer (MISR) description and experiment overview, *IEEE Trans. Geosci. Remote Sens.*, *36*, 1072–1087.

Diner, D. J., R. Davies, T. Várnai, C. Moroney, C. Borel, S. A. W. Gerstl, and D. L. Nelson (1999), Multiangle Imaging SprectroRadiometer (MISR) level 2 top-of-atmosphere albedo algorithm theoretical basis, *JPL Rep. D-13401, Revision D*, 88 pp., Jet Propul. Lab., Pasadena, Calif.

Intergovernmental Panel on Climate Change (2001), *Climate Change 2001: The Scientific Basis: Contribution of Working Group I to the Third Assessment Report of the Intergovernmental Panel on Climate Change*, edited by J. T. Houghton et al., Cambridge Univ. Press, New York.

Kato, S., T. P. Ackerman, J. H. Mather, and E. E. Clothiaux (1999), The k-distribution method and correlated-k approximation for a shortwave radiative transfer model, *J. Quant. Spectrosc. Radiat. Transfer*, *62*, 109–121.

King, M. D., Y. J. Kaufman, W. P. Menzel, and D. Tanre (1992), Remote sensing of cloud, aerosol, and water vapor properties from the moderate resolution imaging spectrometer (MODIS), *IEEE Trans. Geosci. Remote Sens.*, *30*, 2–27.

Loeb, N. G., S. Kato, and B. A. Wielicki (2002), Defining top-of-atmosphere flux reference level for Earth Radiation Budget studies, *J. Clim.*, *15*, 3301–3309.

Loeb, N. G., S. Kato, K. Loukachine, and N. Manalo-Smith (2005), Angular distribution models for top-of-atmosphere radiative flux estimation from the Clouds and the Earth's Radiant Energy System instrument on the Terra satellite. Part I: Methodology, *J. Atmos. Oceanic Technol.*, *22*, 338–351.

Loeb, N. G., S. Kato, K. Loukachine, N. Manalo-Smith, and D. R. Doelling (2006a), Angular distribution models for top-of-atmosphere radiative flux estimation from the Clouds and the Earth's Radiant Energy System instrument on the Terra satellite. Part II: Validation, *J. Atmos. Oceanic Technol.*, in press.

Loeb, N. G., W. Sun, W. F. Miller, K. Loukachine, and R. Davies (2006b), Fusion of CERES, MISR, and MODIS measurements for top-of-atmosphere radiative flux validation, *J. Geophys. Res.*, *111*, D18209, doi:10.1029/2006JD007146.

Stamnes, K., S. C. Tsay, W. J. Wiscombe, and K. Jayaweera (1988), Numerically stable algorithm for discrete-ordinate-method radiative transfer in multiple scattering and emitting layered media, *Appl. Opt.*, *27*, 2502–2509.

Sun, W., N. G. Loeb, and S. Kato (2004), Estimation of instantaneous TOA albedo at 670 nm over ice clouds from POLDER multidirectional measurements, *J. Geophys. Res.*, *109*, D02210, doi:10.1029/2003JD003801.

Suttles, J. T., B. A. Wielicki, and S. Vemury (1992), Top-of-atmosphere radiative fluxes: Validation of ERBE scanner inversion algorithm using Nimbus-7 ERB data, *J. Appl. Meteorol.*, *31*, 784–796.

Vermote, E. F., D. Tanre, J. L. Deuze, M. Herman, and J.-J. Morcrette (1997), Second simulation of the satellite signal in the solar spectrum, 6S: An overview, *IEEE Trans. Geosci. Remote Sens.*, *35*, 675–686.

Wielicki, B. A., B. R. Barkstrom, E. F. Harrison, R. B. Lee III, G. L. Smith, and J. E. Cooper (1996), Clouds and the Earth's Radiant Energy System (CERES): An Earth observing system experiment, *Bull. Am. Meteorol. Soc.*, *77*, 853–868.

Wielicki, B. A., et al. (1998), Clouds and the Earth's Radiant Energy System (CERES): Algorithm overview, *IEEE Trans. Geosci. Remote Sens.*, *36*, 1127–1141.

———————————

R. Davies, Department of Physics, University of Auckland, Private Bag 92019, Auckland 1020, New Zealand.

N. G. Loeb, NASA Langley Research Center, Mail Stop 420, Hampton, VA 23681, USA.

K. Loukachine and W. F. Miller, Science Applications International Corporation, One Enterprise Parkway, Suite 300, Hampton, VA 23666, USA.

W. Sun, Center for Atmospheric Sciences, Hampton University, Hampton, VA 23668, USA. (w.sun@larc.nasa.gov)